Evaluation of FY-4A/AGRI visible reflectance using the equivalents derived from the forecasts of CMA-MESO using RTTOV

Yongbo Zhou[1,2], Yubao Liu[1,2], Wei Han[3,4], Yuefei Zeng[5], Haofei Sun[6], Peilong Yu[5,7,8]

[1]School of Atmospheric Physics, Nanjing University of Information Science & Technology, Nanjing, China

5 [2]Precision Regional Earth Modeling and Information Center (PREMIC), Nanjing University of Information Science & Technology, Nanjing, China

[3]CMA Earth System Modeling and Prediction Centre (CEMC), Beijing, China

[4]State Key Laboratory of Severe Weather (LaSW), Beijing, China

[5]Key Laboratory of Meteorological Disaster of Ministry of Education, Collaborative Innovation Center on Forecast and

10 Evaluation of Meteorological Disasters (CIC-FEMD), Nanjing University of Information Science & Technology, Nanjing, China

[6]Institute of Atmospheric Physics, Chinese Academy of Science, Beijing, China

[7]College of Meteorology and Oceanography, National University of Defense Technology, Changsha, China

[8]High Impact Weather Key Laboratory of CMA, Changsha, China

15 *Correspondence to*: Yongbo Zhou (yongbo.zhou@nuist.edu.cn)

Abstract. The Advanced Geostationary Radiation Imager (AGRI) onboard the FY-4A geostationary satellite provides high spatiotemporal resolution visible reflectance data since 12 March 2018. Data assimilation experiments under the framework of observing system simulation experiments have shown great potential of these data to improve the forecasting skills of numerical weather prediction (NWP) models. To assimilate the AGRI visible reflectance observations, it is important to

20 evaluate the data quality and to correct the biases contained in these data. In this study, the FY-4A/AGRI channel 2 (0.55 μm - 0.75 μm) reflectance data were evaluated by the equivalents derived from the short-term forecasts of the China Meteorological Administration Mesoscale Model (CMA-MESO) using the Radiative Transfer for TOVS (RTTOV, v 12.3). It is shown that the observation minus background (O – B) statistics could be used to reveal the abrupt changes related to the measurement calibration processes. The mean differences of O - B statistics are negatively biased. Potential causes include the NWP model

25 errors, the unresolved aerosol processes, the forward-operator errors, etc. The relative biases of O-B computed for cloud-free and cloudy pixels were used to correct the systematic differences in different conditions. After applying the bias correction method, the biases and standard deviations of O-B departure were reduced. The bias correction based on ensemble forecasts is more robust than deterministic forecasts due to the advantages of the former in dealing with cloud simulation errors. The findings demonstrate that analyzing the O-B departure is effective to monitor the performance of FY-4A/AGRI visible

30 measurements and to correct the associated biases, which facilitates the assimilation of these data in conventional data assimilation applications.

1. Introduction

The Advanced Geostationary Radiation Imager (AGRI) is one of the main payloads onboard the FY-4A, the first of the new-generation Chinese geostationary meteorological satellites lunched on 11 December 2016 (Yang et al., 2017).

FY-4A/AGRI contains seven shortwave channels and seven infrared channels. The FY4A/AGRI data have been widely used for retrieving cloud optical thickness (Chen et al., 2020), total precipitable water (Liu et al., 2022), and aerosol optical depth (AOD) (Ding et al., 2022). In addition, the FY-4A infrared radiance data were assimilated into Numerical Weather Prediction (NWP) models, and positive impact on the forecasts of Typhoon cases (Zhang et al., 2022) and Heavy rainfall events (Xu et al., 2023) was reported. The FY-4A/AGRI visible radiance data were also assimilated into NWP models in an observation system simulation experiment (OSSE) framework, and the results revealed positive impact on cloud variables and some slightly positive impact on non-cloud variables in the vicinity of cloudy regions (Zhou et al., 2022; Zhou et al., 2023).

The AGRI, with minor improvements by including an extra infrared channel, was also equipped to FY-4B lunched on 3 June, 2021, which is the second of the new-generation Chinese geostationary meteorological satellites. FY-4A and FY-4B are located at 104.7 °E and 133.0 °E separately. The two satellites cover a large part of the East Asian and Western Pacific, providing rich visible and infrared radiance data that are highly valuable for data assimilation applications.

Data assimilation of AGRI data in real cases demands accurate analysis of observation errors, including the biases and the Probability density Distribution Function (PDF) of the observation errors. On one hand, conventional data assimilation methods assume that the observations are unbiased and the PDF of the observation errors conforms to a Gaussian function (Geer and Bauer, 2011; Bonavita et al., 2016; Li et al., 2022). On the other hand, the magnitude of the observation errors influences the data assimilation results by tuning the weights given to each observation. Several methods were involved to characterize the observation errors of satellite data and an inter-comparison method between the satellite observations and the equivalents derived from the forecasts of NWP models using forward operators receives general popularity (Auligné et al., 2007; Zou et al., 2016; Lu et al., 2020; Noh et al., 2023). The inter-comparison method was applied to characterize the error statistics of FY-4A/AGRI infrared channels under cloud-free and cloudy conditions (e.g. Geng et al., 2018; Xu et al., 2023). To the best of our knowledge, the method has not yet been applied to characterize the error characteristics of FY-4A/AGRI visible reflectance data within any data assimilation systems.

The key assumption of the inter-comparison method is that the model equivalents do not generate systematic biases and thus can be deemed as reference. The accuracy of the model equivalents depends on many factors involving the NWP model and the forward operator (Janjić et al., 2017). A NWP model faces challenges to generate realistic representative atmosphere state variables due to its inherent limitations such as the inadequacies of microphysical schemes, the uncertainties of the initial conditions (ICs) and lateral boundary conditions (LBCs), etc. The NWP model errors could be alleviated either by assimilating synthetic observations by improved data assimilation methods, or by temporally averaging several instants over a long period

of time (Scheck et al., 2018), or by ensemble forecasts which involve several microphysics combinations or different ICs and

LBCs (Li et al., 2015). In addition, a forward operator inevitably suffers from errors due to the uncertainties of cloud optical

65 properties (Zhou et al., 2018), aerosol-cloud interactions (Geiss et al., 2021), etc. To save computational cost,

three-dimensional (3D) radiative processes were usually simplified into one-dimensional (1D) processes (e.g., the independent

column approximation, IPA), which is another source of forward-operator errors. The main factors which contribute to the

simulation errors of the reflectance equivalents should be properly assessed to increase the robustness of the inter-comparison

results.

70   In this study, the FY-4A/AGRI channel 2 reflectance data were evaluated by comparing the observations and the

equivalents derived from the forecasts of the China Meteorological Administration Mesoscale Model (CMA-MESO) using the

Radiative Transfer for TOVS (RTTOV, v 12.3). CMA-MESO is warm-started by assimilating comprehensive observations

and thus provides high-quality background state variables. The main purpose of this study is to address the following two

questions. First, is analyzing the observations minus background equivalents (O-B departure, hereafter) an effective way to

75 monitor the performance of FY-4A/AGRI visible instrument? Second, what are the characteristics of the biases of O-B

departure and how to correct them? In viewing of these two questions, the remaining part of this manuscript is organized as

follows. Data and method are introduced in Section 2. The statistics of the O-B departure and the influences of some main

factors are presented in Section 3. A bias correction method is promoted in Section 4. Conclusions are summarized in Section

5.

80 **2. Data and method**

2.1 Simulated CMA-MESO visible reflectance

Simulated visible reflectance was generated from 3-h forecasts of the CMA-MESO model with a horizontal grid spacing of

0.03 °×0.03 °. The CMA-MESO forecasts cover the period from 1 September 2020 to 29 September 2020 at 06:00 UTC.

Therefore, the CMA-MESO forecasts were initialized from the analyses at 03:00 UTC, which were generated by assimilating

85 the cloud motion wind retrieved from FY-2G and Himawari-8 satellite observations, the Global Navigation Satellite System

(GNSS) radio occultation (RO) data, the FY-4A/AGRI clear-sky infrared radiances, etc (Shen et al., 2020). The comprehensive

observations were assimilated by a three-dimensional variational (3DVar) data assimilation system.

The physics configurations of CMA-MEAO include the Single–Moment 6–class microphysical scheme (Hong and Lim,

2006), the Meso-SAS (Simplified Arakawa-Schubert) Cumulus Parameterization option (Zhang et al., 2017), and the Yonsei

90 University (YSU) planetary boundary layer scheme (Hong and Lim, 2006; Hu et al., 2013), the Unified Noah land surface

scheme (Tewari et al., 2004), the Rapid Radiative Transfer Model for Global Climate Models (RRTMG) longwave and

shortwave radiation schemes (Iacono et al., 2008). The model configurations generate non-cloud variables (water vapor

mixing ratio, temperature, etc) and cloud variables including the mixing ratio of five cloud hydrometeors (cloud droplet, rain, ice, snow, and graupel) and cloud cover. To facilitate the radiative transfer simulations, the effective radius of cloud liquid

95 droplets was calculated following Thompson et al. (2004) and Yao et al. (2018).

The mixing ratios of cloud hydrometeors were used to identify whether a column is cloudy or cloud-free. The column was assumed to be cloud-free when the cloud water path (CWP, the vertically integrated cloud mixing ratio of the five hydrometeors) is less than 0.01 kg m^{-2}. Otherwise, the column was assumed to be cloudy. The cloud masks were used for the bias correction for cloud-free and cloudy pixels, separately.

100 The 3-h forecasts of CMA-MESO were processed into the format of the RTTOV input files. The solar and satellite zenith angles and azimuth angles were provided by the FY-4A synchronous observation geometry (GEO) data gridded at 4km × 4km resolution, which were interpolated to the location of the CMA-MESO simulations. The liquid and ice cloud optical properties in RTTOV were parameterized by the "Deff" scheme (Mayer and Kylling, 2005) and the Baran et al. (2014) scheme, respectively. The layer-to-space transmittance was computed by the v9 predictors on 54 levels (Matricardi, 2008). The surface

105 Bidirectional Reflectance Distribution Function (BRDF) was drawn from the land surface atlases (Vidot and Borbás, 2014; Vidot et al., 2018) or calculated by the JONSWAP model for the sea surface (Hasselmann et al., 1973). The radiative transfer processes were solved by the Discrete Ordinate Method (DOM).

2.2 FY-4A/AGRI observations

To generate spatially matched pairs of observations and backgrounds, the FY-4A/AGRI full-disk channel 2 reflectance data

110 gridded at 1 km×1 km resolution were horizontally averaged to the CMA-MESO locations. The horizontal averaging was performed by the following two procedures. Firstly, centering at a given CMA-MESO grid point and find all the pixels (matched pixels hereafter) in the FY-4A/AGRI visible imagery within ±0.015° both in the zonal and meridional directions. Secondly, averaging the reflectances of all these matched pixels to generate a reflectance that is spatially matched to the CMA-MESO grid. Repeating the two steps for all CMA-MESO grid points generated an observed imagery gridded at

115 0.03°×0.03°. In addition, the maximum allowable time differences between the FY-4A observations and CMA-MESO forecasts are within 15 minutes to ensure temporal match.

The FY-4A cloud mask (CLM) product was used to indicate whether a pixel of observed imagery is cloudy or cloud-free. The CLM product is gridded at 4 km×4 km resolution. Unlike the GEO data which provides continuous data, CLM product contains discrete values. Therefore, the 4 km×4 km CLM data were matched to the CMA-MESO location by the least-distance

120 matching that was performed by finding the pixel of the CLM data which has the least distance with the CMA-MESO grid.

After applying the above processes to the FY-4A observations, the FY-4A visible reflectance data and CLM data were spatially matched to the CMA-MESO simulations, which facilities the analysis of O-B statistics. Figure 1 shows an example of

the FY-4A/AGRI observations matched to the CMA-MESO locations, including the visible reflectance of channel 2, cloud

mask, solar zenith angle, solar azimuth angle, satellite zenith angle, and satellite azimuth angle.
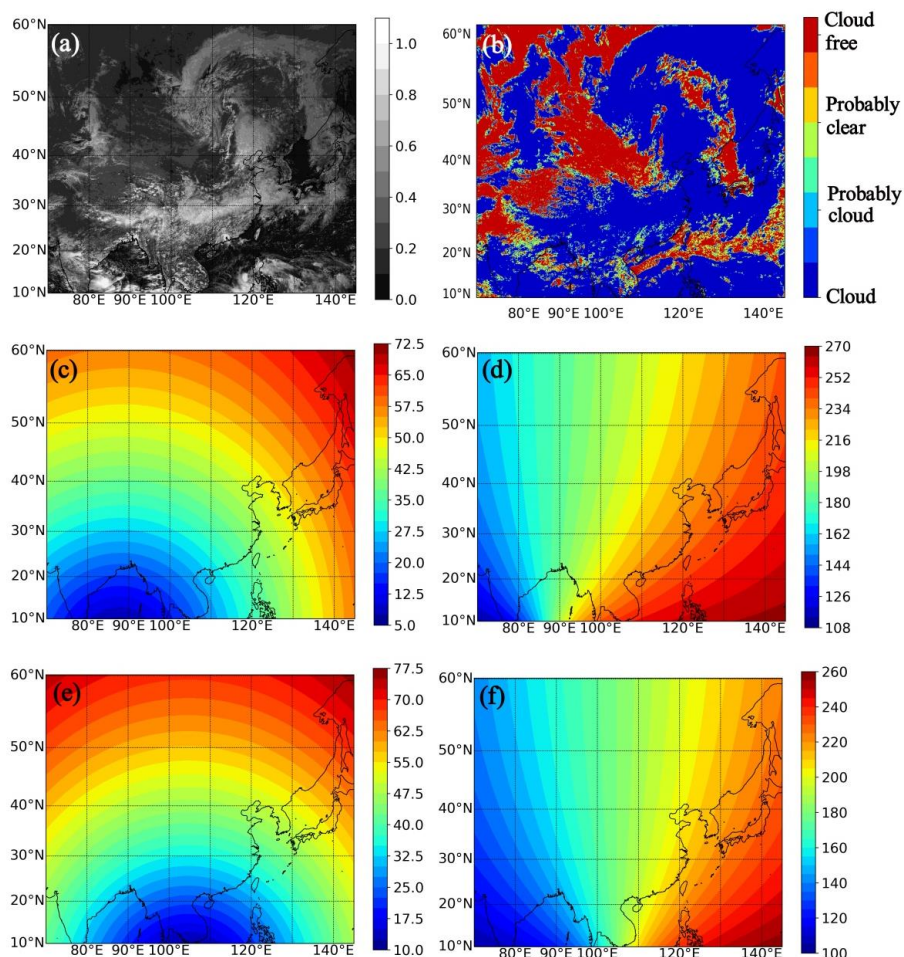
125

Figure 1: FY-4A/AGRI observations at 06:00 UTC on 15 September 2020, which were matched to the CMA-MESO locations. (a) Reflectance at 0.65 μm; (b) Cloud mask; (c) Solar zenith angle; (d) Solar azimuth angle; (e) Satellite zenith angle; (f) Satellite azimuth angle.

3. O-B statistics and main contributing factors

130 **3.1 The bias of O-B departure**

The one-month temporal variation of the mean differences of O-B revealed that the O-B departure was positively biased (Fig.

2). The O-B departure was collaboratively influenced by many factors. Since these factors may interact with other, it is difficult

to draw a definitive conclusion whether the observations were overestimated or the background equivalents were

underestimated or the both. Nevertheless, the abrupt change of the bias from September 9th to 10th was more likely caused by

135   the measurement errors rather than the background errors since no quick-developing weather system was reported during this

period of time. In fact, the calibration correction coefficients of FY-4A/AGRI channel 2 were updated by the National Satellite

Meteorological   Center   of   CMA   at   02:00   UTC   on   9   September   2020

(http://gsics.nsmc.org.cn/portal/cn/event/AGRI.html?satellite=FY4A). The finding answers the first question that analyzing

the O-B departure is an effective way to monitor the performance of the FY-4A visible instruments.
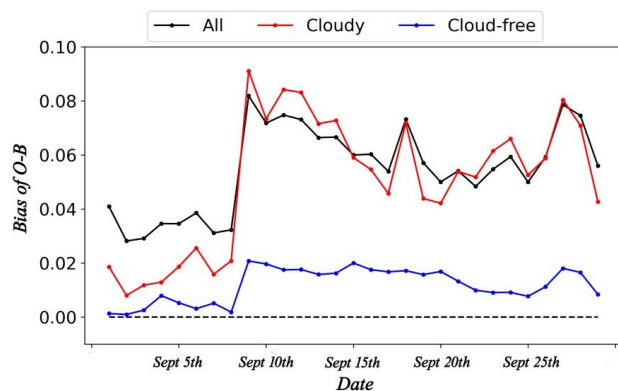
140

Figure 2: The temporal variation of the mean differences of O-B departure for cloud-free, cloudy and all pixels.

3.2 Influences of the NWP forecasts

Since the visible reflectance is particularly sensitive to cloud properties, the statistics of O-B departure is determined to a large

extent by the forecasts of NWP models. To illustrate this, the deterministic forecast (3-h lead time) at 06:00 UTC on 15

145   September 2020 was compared with an ensemble forecast which includes 7 ensemble members, with each ensemble member

corresponding to a lead time of 3 h, 6 h, 9 h, 12 h, 15h, 18 h, and 21 h, respectively. The deterministic forecast and the ensemble

forecast were utilized to derive the equivalent reflectance and ensemble mean reflectance, denoted by B and $\overline{B}$, respectively.

The results indicated distinct differences between B and $\overline{B}$ (Fig. 3) and between the statistics of O-B and O-$\overline{B}$. As is shown in

Fig. 1(a) and Fig. 3, the underestimation of cloud cover in the deterministic forecast was alleviated in the ensemble forecast.

150   This is not surprising, as it can be expected that an ensemble forecast should have advantages over a deterministic forecast in

dealing with cloud displacement errors and in simulating cloud microphysical properties.
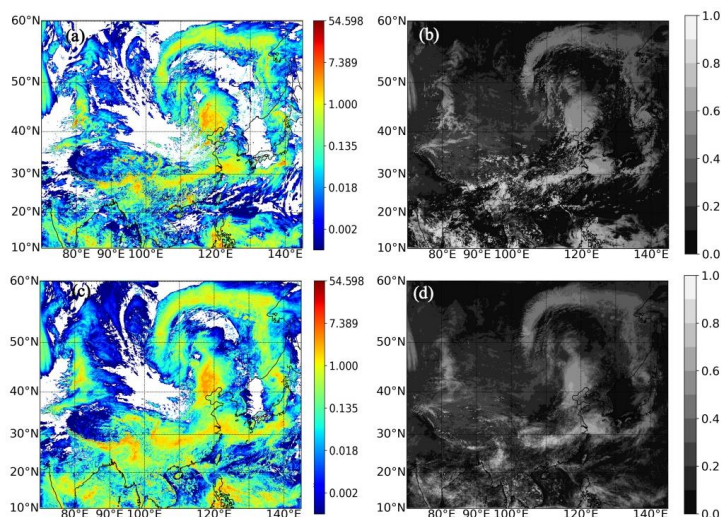
Figure 3: Cloud water path and the reflectance derived from a deterministic forecast and an ensemble forecast at 06:00 UTC on 15 September 2020. (a) Cloud water path for the deterministic forecast; (b) Reflectance derived from deterministic forecast; (c)
155 **Ensemble mean of the cloud water path for the ensemble forecast including seven ensemble members; (d) Ensemble mean of the reflectance derived from the ensemble forecast including seven ensemble members.**

3.3 Influences of unresolved aerosol processes

The aerosol processes cannot be properly resolved by the CMA-MESO model. However in real cases, aerosols have significant impact on the observed reflectance, which is the theoretical basis for the remote sensing of AOD by satellite measurements. To
160 evaluate the impact of aerosols on the top-of-atmosphere (TOA) reflectance, a sensitivity study was performed by RTTOV with varying aerosol optical properties based on the 3-h forecast of CMA-MESO at 06:00 UTC on 15 September 2020. The aerosols were assumed to decrease with height in an Exponential function with a scale height of 2.0 km. The optical properties of aerosols were configured with those of the dust aerosol of Cloud-Aerosol Lidar and Infrared Pathfinder Satellite Observation (CALIPSO) (Omar et al., 2009). The optical properties of the dust aerosol at the center wavelength of
165 FY-4A/AGRI channel 2 were calculated by logarithmic interpolation of the optical properties at 0.532 μm and 1.064 μm provided by Zhou et al. (2017). The logarithmic interpolation was also used to supply the AOD out of the reference wavelengths in the SBDART radiative transfer model (Ricchiazzi et al., 1998).

The impact of dust aerosols on TOA reflectance is demonstrated by Fig. 4. The results indicate that the impact of aerosols on the TOA reflectance is highly dependent on AOD and CWP (As a general approximation, CWP is positively related to the
170 TOA reflectance). Under cloud-free conditions, the presence of dust aerosols tends to increase the TOA reflectance due to the fact that dust aerosols scatter some photons to the satellite sensors. With the increase of CWP, the impact of dust aerosols tends to generate negative bias on the TOA reflectance. A potential explanation is that dust aerosols absorb some photons from the incoming path to clouds and from the outgoing path to satellite. The two-fold impact of aerosols was also reported by Geiss et

al (2021). The impact of aerosols was also influenced by aerosol types and aerosol vertical distribution structures (not shown

175   for simplicity).
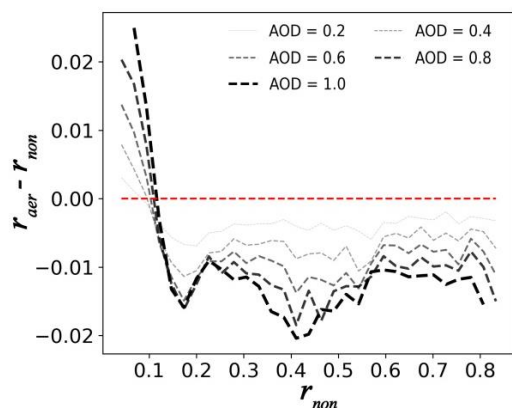
Figure 4: The impact of dust aerosols on the TOA reflectance. r_{non} **denotes the reflectance simulated by RTTOV based on cloud profiles derived from the 3-h forecast at 06:00 UTC on 15 September 2020.** r_{aer} **denotes the reflectance based on cloud profiles and dust aerosols.**

180   **3.4 Influences due to forward-operator errors**

The forward-operator errors include errors due to numerical discretization when solving the radiative transfer equations, errors in cloud optical properties, etc. The impact of cloud optical properties was illustrated by a sensitivity study performed by RTTOV configured with the SSEC/Baum ice scheme (Baum et al., 2011) based on the 3-h forecast of CMA-MESO at 06:00 UTC on 15 September 2020. The results indicate that the TOA reflectance simulated by SSEC/Baum ice scheme was

185   underestimated compared with that simulated by the ice scheme of Baran et al (2014) (Fig. 5), which imply the uncertainties in the cloud optical properties of RTTOV.
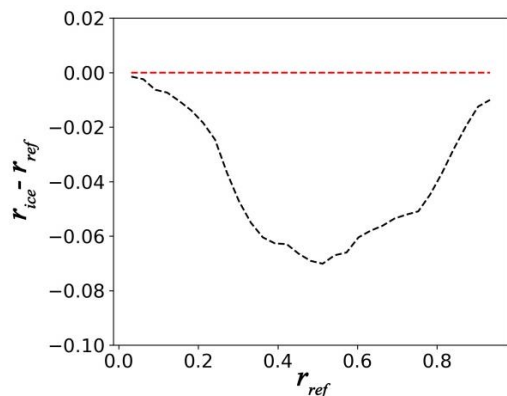
Figure 5: The impact of ice cloud schemes on the TOA reflectance. r_{ref} **denotes the reflectance simulated by RTTOV configured with the ice scheme of Baran et al. (2015).** r_{ice} **denotes the simulations based on the SSEC/Baum ice scheme.**

190   As is mentioned above, 3D radiative effects also contribute to the forward-operator errors and they could be alleviated by increasing the model grid spacing (V árnai and Marshak, 2001; Zinner et al., 2006) or simply by horizontally averaging of the

pixels (Kostka et al., 2014). However, small-scale properties could not be properly resolved with large grid spacing or could be cancelled out for the observations averaged over $n \times n$ pixels (n denotes the number of pixels involved). In view of this, the horizontal averaging was not performed to the 0.03 °×0.03 °forecasts or the observations.

195   **4. Bias correction**

As is shown in Section 3, there are some systematic biases in the O-B departure. In cycled data assimilation of satellite infrared and microwave data, the equivalents derived from the first-guess state variables are used as a reference to correct the observations. Some well-designed predictors such as the average cloud impact (Harnisch et al., 2016) or the NWP model state variables (Noh et al., 2023) were regressed to the O-B departure and the systematic differences were corrected based on the

200   regression.

Compared with the infrared and microwave radiance observations, the visible reflectance is much more sensitive to cloud variables, regardless of the type of cloud hydrometeors or the vertical location of clouds. However, the infrared radiance data are mostly sensitive to cloud top and the microphysical properties therein (Li et al., 2022) or to the clouds which are above the peaks of the weighting functions of the infrared channels (Harnisch et al., 2016). The microwave radiance data are insensitive

205   to small cloud hydrometeors and were usually used to restraint large particles such as rain drops (Wang et al., 2021). In addition, the visible reflectance is less sensitive to temperature or humidity compared with the infrared and microwave radiances. Since the NWP model errors are particularly evident in cloudy conditions (Mathiesen and Kliessl, 2011) and the predictor-based bias correction is largely determined by the equivalents derived from NWP forecasts, the robustness of the predictor-based bias correction method should be reduced when applied to the visible bands.

210   In view of the analyses above, the systematic biases in O-B was simply corrected by the first-order approximation method promoted by Harnisch et al (2016), i.e., the mean differences of O-B, denoted by $\overline{O-B}$ where the bar denotes the domain-averaged value. It is noted that the first-order approximation of the O-B was depicted by $(\overline{O-B})/\overline{O}$ rather than $\overline{O-B}$ to avoid generating reflectance beyond the 0~1 range during the bias correction. Therefore, the corrected reflectance is calculated by Eq. (1),

215    $$O' = O(1 - \gamma) \tag{1}$$

where γ denotes the bias correction coefficient.

$(\overline{O-B})/\overline{O}$ is denoted by μ_{clr} (or μ_{cld}) for the pixels which are cloud-free (or cloudy) for both the observations and the derived equivalents. To correct the biases in observations according to Eq. (1), γ was set to μ_{clr} (or μ_{cld}) for the pixels which were masked to be cloud-free (or cloudy) in the observed imagery. For pixels with uncertain cloud mask in the observed

220   imagery, γ was set to $(\mu_{clr} + \mu_{cld})/2$.

The bias correction was tested by three selected cases on September 1st, 15th, and 17th, 2020. The three cases cover the observations before and after the update of the calibration coefficients on 9 September 2020. Quantitative analysis of the O-B statistics indicates that the bias correction method is effective in reducing the means and standard deviations of O-B (Tables 1 and 2). In general, the discrepancies between O and B were mainly revealed in cloudy conditions. The bias-corrected visible

225 imagery (Fig. 6(b1-b3)) maintains the general spatial distribution characteristics of the raw imagery (Fig. 1a). For the bias correction based on a deterministic forecast, the right-side tail of the PDF of O-B shrank, while opposite impact was introduced to the left side of the PDF (Fig. 7). The results imply that despite of the general positive impact, the bias correction based on a deterministic forecast is mostly effective in correcting the biases when the observations are overestimated. The reason is that the bias correction method is designed to extend μ_{cld} in cloudy pixels for both O and B to the cloudy pixels only for O. Such

230 extension was accompanied with cloud simulation errors, e.g., the pixel with thick cloud in O could correspond to a pixel with thin cloud or clear sky in B.

Table 1: The mean differences of the observations minus equivalents. The comparison takes into account observations with and without bias correction, and the equivalents derived from deterministic forecasts and ensemble forecasts.

Forecasts		deterministic forecast			ensemble forecast		
cloud mask		clear	cloudy	all	clear	cloudy	all
09-01	uncorrected	-0.0088	0.0617	0.0409	-0.0115	0.0719	0.0458
	corrected	-0.0101	0.0447	0.0288	-0.0049	0.0202	0.0119
09-15	uncorrected	0.0075	0.0864	0.0600	0.0049	0.0988	0.0662
	corrected	-0.0129	0.0316	0.0169	-0.0076	0.0140	0.0051
09-17	uncorrected	0.0045	0.0795	0.0540	0.0005	0.0969	0.0629
	corrected	-0.0117	0.0378	0.0211	-0.0075	0.0183	0.0073

Table 2: The standard deviations of the observations minus equivalents. The comparison takes into account observations with and without bias correction, and the equivalents derived from deterministic forecasts and ensemble forecasts.

235

Forecasts		deterministic forecast			ensemble forecast		
cloud mask		clear	cloudy	all	clear	cloudy	all
09-01	uncorrected	0.0690	0.1878	0.1658	0.0532	0.1461	0.1315
	corrected	0.0690	0.1845	0.1621	0.0534	0.1326	0.1165
09-15	uncorrected	0.0661	0.2158	0.1862	0.0532	0.1751	0.1540
	corrected	0.0656	0.2029	0.1736	0.0523	0.1486	0.1273
09-17	uncorrected	0.0680	0.2086	0.1819	0.0568	0.1680	0.1511
	corrected	0.0670	0.2015	0.1741	0.0558	0.1491	0.1296
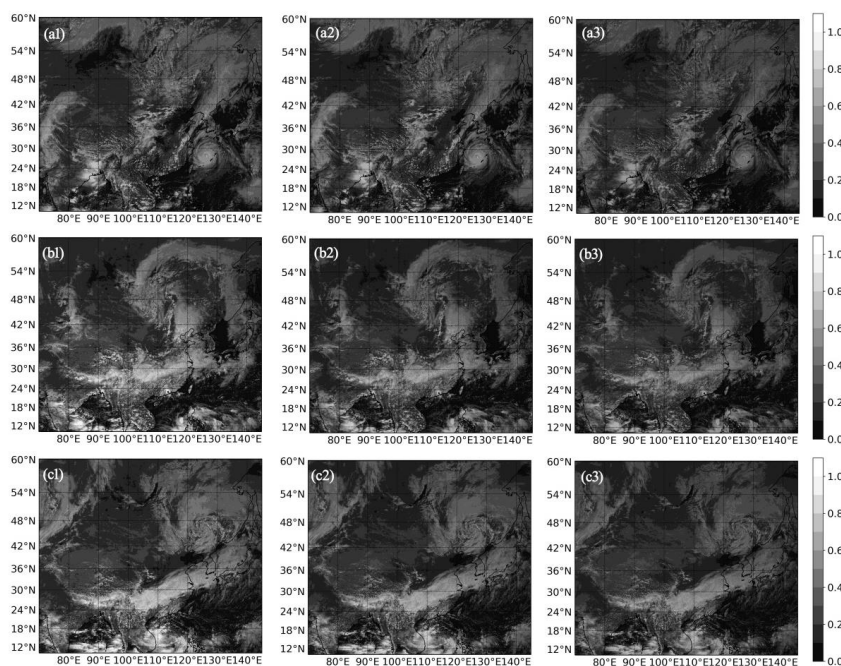
Figure 6: The observed and bias-corrected reflectance at 06:00 UTC on 1 September 2020 (a1-a3), 15 September 2020 (b1-b3), and 17 September 2020 (c1-c3). From left to right, the three columns correspond to the observed reflectance, the bias-corrected reflectance based on a deterministic forecast, and the bias-corrected reflectance based on an ensemble forecast.

240   The ensemble forecast is believed to be an effective way to mitigate cloud simulation errors and their subsequent negative impact on the bias correction. To correct the biases based on ensemble forecasts, μ_{clr} and μ_{cld} were set to $\overline{(O - \overline{B})/\overline{O}}$ for the pixels which are masked to be cloud-free and cloudy both for O and $\overline{B}$. Better results were revealed in the statistics of O-$\overline{B}$ (Tables 1 and 2) and in the left side of the PDF than the bias correction based on the deterministic forecast (Fig. 7). Therefore, ensemble forecasts increase the robustness of the bias correction method based on the domain-averaged relative differences

245   between observations and equivalents.
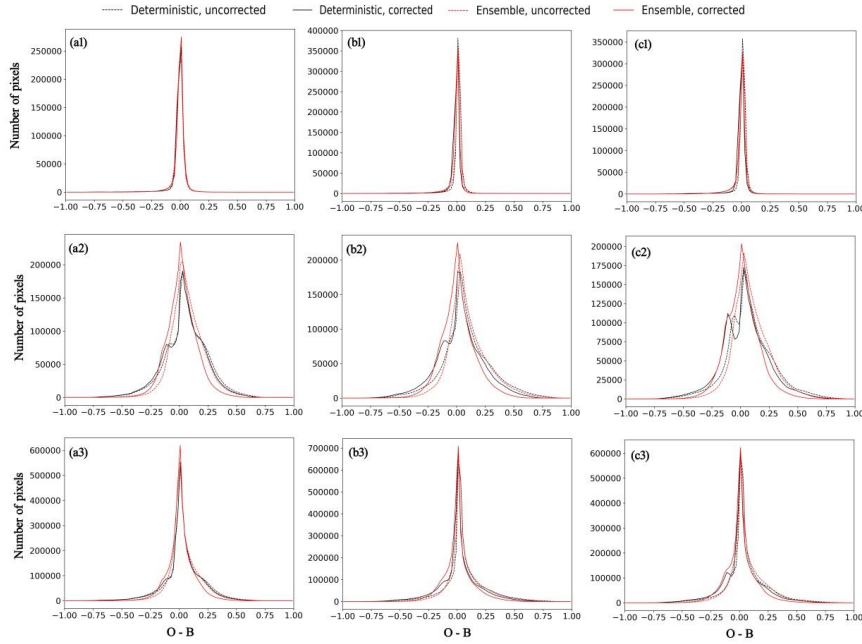
Figure7: The probability density distribution function of O-B departure of visible reflectance. From left to right, the columns correspond to the results for 1 September 2020, 15 September 2020, and 17 September 2020, respectively. From top to bottom, the rows correspond to the results for cloud-free, cloudy, and all pixels.

250   The pseudocode for the bias correction method based on the equivalents derived from ensemble forecasts was illustrated by the following:

$$\mu_{clr} \leftarrow \frac{\sum_{k=1}^{N_{clr}}\left(O_k^{clr} - \overline{B_k^{clr}}\right)}{\sum_{k=1}^{N_{clr}}\left(O_k^{clr}\right)} \quad \#\#\#N_{clr}: \text{the number of cloud-free pixels for both O and } \overline{\text{B}}$$

$$\mu_{cld} \leftarrow \frac{\sum_{k=1}^{N_{cld}}\left(O_k^{cld} - \overline{B_k^{cld}}\right)}{\sum_{k=1}^{N_{cld}}\left(O_k^{cld}\right)} \quad \#\#\#N_{cld}: \text{the number of cloudy pixels for both O and } \overline{\text{B}}$$

$$\mu_{uct} = (\mu_{clr} + \mu_{cld})/2$$

for $m = 1$: N_{obs} **do** ## N_{obs} denotes the number pixels in **O**

255   **if** $cld\_mask(m) == 3$ **then** ### for cloud-free pixels

$$o'_m \leftarrow o_m(1 - \mu_{clr})$$

else if $cld\_mask(m) == 0$ **then** ### for cloudy pixels

$$o'_m \leftarrow o_m(1 - \mu_{cld})$$

else:

$$o'_m \leftarrow o_m(1 - \mu_{uct})$$

end if

end for

260   **5. Conclusions**

In this study, the FY-4A/AGRI channel 2 visible reflectance data in September 2020 were evaluated by the equivalents derived from the forecasts of the CMA-MESO model using RTTOV radiative transfer model. The temporal variation of the observation minus background (O-B) statistics was evaluated, and main error sources were analyzed. In addition, a bias correction method was developed to ensure that the FY-4A/AGRI observation was unbiased and the PDF of the observation

265   errors is subject to a Gaussian function, which will facilitate the data assimilation application of FY-4A/AGRI reflectance data. The main findings are summarized below.

Compared with B, O was positively biased. The temporal variation characteristics of biases revealed an abrupt change on 9 September 2020, when the calibration correction coefficient of FY-4A/AGRI channel 2 was updated by the National Satellite Meteorological Center. The findings indicate that the reflectance derived from the CMA-MESO forecasts was capable of

270   monitoring the performance of the FY-4A visible instruments, which was the normal routine for monitoring the infrared and microwave instruments in National Satellite Meteorological Center of China and other satellite instrument monitoring systems (Lu et al., 2020).

Apart from the measurement errors, the influences of forward-operator errors and NWP model errors were assessed by sensitivity studies. The forward-operator errors were especially evident for cloudy pixels since RTTOV suffers uncertainties in

275   cloud optical properties. The impact of aerosols on O was not considered in B because CMA-MESO is unable to resolve aerosol processes currently. Sensitivity studies indicate that neglecting aerosols tends to decrease the TOA reflectance in cloud-free conditions. In cloudy conditions, the impact of aerosols was complicated by aerosol type and aerosol vertical distribution.

Despite that O-B was collaboratively determined by many factors, systematic differences between O and B were revealed,

280   which facilitates the bias correction in data assimilation applications. The goal of the bias correction in data assimilation is to minimize the differences between O and B. Unlike the bias correction of infrared and microwave radiance data based on some well-designed predictors, the biases in visible reflectance data were simply corrected by the domain-averaged relative differences of O-B. The main reason is that the predictor-based bias correction could introduce extra errors in the background to the observations since the visible equivalents are largely influenced by uncertainties in background which are particularly

285   evident in cloudy regions. Validation of the bias correction method indicated that the biases and uncertainties of O-B were decreased after applying the bias correction method. Since ensemble forecasts have great advantages over deterministic forecasts in reducing cloud simulation errors, the Gaussian distribution of PDF of O-B was better respected based on the equivalents derived from an ensemble forecast. Therefore, it is recommended to generate the reflectance equivalents from ensemble forecasts when correcting the biases in visible reflectance data.

290   It is noted that the equivalents derived from a deterministic forecast or an ensemble forecast are inevitably associated with simulation errors both in the NWP models and forward operators. Since it is impossible to eliminate all sources of errors, the bias correction method should be particularly effective when the simulation errors are eradicated. Nevertheless, the simulation errors could be mitigated by more accurate forward operators (e.g. forward operators which accounts for three-dimensional radiative effects) and more representative background state variables (e.g., short-term forecasts based on advanced data

295   assimilation method, ensemble forecasts which involve multiple microphysical configurations, etc). Extending the above-mentioned methods to data assimilation applications is ongoing.

Code availability. Version 12.3 of RTTOV source code is publicly available at https://nwp-saf.eumetsat.int/site/software/rttov/rttov-v12/ (last access: 5 March 2019).

Data availability. The CMA-MESO short-term forecasts data in 2020 were provided by the CMA Earth System Modeling and

300   Prediction Centre (CEMC). The FY-4A/AGRI 1km×1km full-disk reflectance data, the 4km ×4km geometry (GEO) data and cloud mask products are obtained from the National Satellite Meteorological Center (NSMC) at http://satellite.nsmc.org.cn/PortalSite/Data/DataView.aspx?currentculture=zh-CN. The datasets are also available upon request from Yongbo Zhou (yongbo.zhou@nuist.edu.cn).

Author contribution. YZ devised the methodology, performed radiative transfer simulations using RTTOV, downloaded and

305   processed the FY-4A/AGRI data, realised and evaluated the experiment, and wrote the paper. YL supervised the research activity and provided the linux cluster for radiative transfer simulations and related calculations. WH and HS provided the CMA-MESO short-term forecasts and some guidance on the processing of these data. YZ evaluated the experiment designs and revised the writing. All authors were involved in discussions throughout the development and experiment phase, and all authors commented on the paper.

310   *Competing interests.* The contact author has declared that none of the authors has any competing interests

Acknowledgement. The authors acknowledge the financial support of the National Natural Science Foundation of China (No. 42305161), the Natural Science Foundation of Jiangsu Province (No. BK0210665), and the Startup Foundation for Introducing Talent of Nanjing University of Information Science and Technology (Grant No. 2019r095). In addition, we acknowledge the High Performance Computing Center of Nanjing University of Information Science & Technology for their support of this

315   work.

Financial support. This research has been supported by the National Natural Science Foundation of China (No. 42305161), the Natural Science Foundation of Jiangsu Province (No. BK0210665), and the Startup Foundation for Introducing Talent of Nanjing University of Information Science and Technology (Grant No. 2019r095).

References

320   Auligné, T., McNally, A. P., and Dee, D. P.: Adaptive bias correction for satellite data in a numerical weather prediction system, Q. J. R. Meteorol. Soc., 133: 631-642, doi: 10.1002/qj.56, 2007.

Baran, A. J., R. Cotton, K. Furtado, S. Havemann, L.-C. Labonnote, F. Marenco, A. Smith, and Thelen, J.-C.: A self-consistent scattering model for cirrus. II: The high and low frequencies, Q. J. R. Meteorol. Soc., 140, 1039-1057, doi: 10.1002/qj.2193, 2014.

325   Baum, B. A., Yang, P., Heymsfield, A. J., Schmitt, C., Xie, Y., Bansemer, A., Hu, Y. X., and Zhang, Z.: Improvements to shortwave bulk scattering and absorption models for the remote sensing of ice clouds, J. Appl. Meteorol. Clim., 50, 1037–1056, doi: 10.1175/2010JAMC2608.1, 2011.

Bonavita, M., , Hólm. E., Isaksen. L., and Fisher, M.: The evolution of the ECMWF hybrid data assimilation system, Q. J. R. Meteorol. Soc., 142, 287–303, doi: 10.1002/qj.2652, 2016.

330   Chen, Y., Chen, G., Cui, C., Zhang, A., Wan, R., Zhou, S., Wang, D., and Fu, Y.: Retrieval of the vertical evolution of the cloud effective radius from the Chinese FY-4 (Feng Yun 4) next-generation geostationary satellites, Atmos. Chem. Phys., 20, 1131–1145, doi: 10.5194/acp-20-1131-2020, 2020.

Ding, H., Zhao, L., Liu, S., Chen, X., de Leeuw, G., Wang, F., Zheng, F., Zhang, Y., Liu, J., Li, J., She, L., Si, Y. and Gu, X.: FY-4A/AGRI Aerosol Optical Depth Retrieval Capability Test and Validation Based on NNAeroG, Remote Sens., 14, 5591,

335   doi: 10.3390/rs14215591, 2022.

Geer, A. J., and Bauer, P.: Observation errors in all-sky data assimilation, Q. J. R. Meteorol. Soc., 137, 2024-2037, doi: 10.1002/qj.830, 2011.

Geiss, S., Scheck, L., de Lozar, A., and Weissmann, M.: Understanding the model representation of clouds based on visible and infrared satellite observations, Atmos. Chem. Phys., 21, 12273–12290, doi: 10.5194/acp-21-12273-2021, 2021.

340   Geng, X., Min, J., Yang, C., Wang, Y., and Xu, D.: Analysis of FY-4A AGRI bias characteristics and correction experiment, Chinese J. Atmos. Sci. (in Chinese), 44(4): 679-694, doi: 10.3878/j.issn.1006-9895.1907.18254, 2018.

Hasselmann, K., Barnett, T. P., Bouws, E., Carlson, H., Cartwright, D. E., Enke, K., Ewing, J. A., Gienapp, H., Hasselmann, D. E., Kruseman, P., Meerburg, A., Müller, P., Olbers, D. J., Richter, K., Sell, W., and Walden, H.: Measurements of wind-wave growth and swell during the Joint North Sea Wave Project (JONSWAP), Dtsch. Hydrogr. Z., 8, 1–95,

345   http://resolver.tudelft.nl/uuid:f204e188-13b9-49d8-a6dc-4fb7c20562fc (last access: 23 September 2022), 1973.

Harnisch, F., Weissmann, M., and Periáñez, Á.: Error model for the assimilation of cloud-affected infrared satellite observations in an ensemble data assimilation system, Q. J. R. Meteorol. Soc., 142: 1797–1808, doi:10.1002/qj.2776, 2016.

Hong, S.-Y. and Lim, J.-O. J.: The WRF single-moment 6-class microphysics scheme (WSM6), J. Korean Meteor. Soc., 42, 129–151, 2006.

350   Hu, X. M., Klein, P.M., and Xue, M.: Evaluation of the updated YSU planetary boundary layer scheme within WRF for wind resource and air quality assessments, J. Geophys. Res., 118, 10490–10505, doi: 10.1002/jgrd.50823, 2013.

Iacono, M. J., Delamere, J. S., Mlawer, E. J., Shephard, M. W., Clough, S. A., and Collins, W. D.: Radiative forcing by long-lived greenhouse gases: Calculations with the AER radiative transfer models, J. Geophys. Res., 113, D13103, doi:10.1029/2008JD009944, 2008.

355   Janjić, T., Bormann, N., Bocquet, M., Carton, J. A., Cohn, S. E., Dance, S. L., Losa, S. N., Nichols, N. K., Potthast, R., Waller, J. A., and Weston, P.: On the representation error in data assimilation, Q. J. R. Meteorol. Soc., 144(713), 1257–1278, doi: 10.1002/qj.3130, 2017.

Kostka, P. M., Weissmann, M., Buras, R., Mayer, B., and Stiller, O.: Observation operator for visible and near-infrared satellite reflectances, J Atmos. Oceanic. Technol., 31(6):1216–33, doi: 10.1175/JTECH- D- 13- 00116.1, 2014.

360   Liu, X., Wang, Y., Huang, J., Yu, T., Jiang, N., Yang, H. and Zhan, W.: Assessment and calibration of FY-4A AGRI total precipitable water products based on CMONOC, Atmos. Res., 271, 106096, doi: 10.1016/j.atmosres.2022.106096, 2022.

Li, J., Du, J., and Liu, Y.: A comparison of initial condition-, multi-physics- and stochastic physics-based ensembles in predicting Beijing "7.21" excessive storm rain event, Acta Meteorologica Sinica (in Chinese), 73(1): 50-71. doi: 10.11676/qxxb2015.008, 2015.

365   Li, J., Geer, J. A., Okamoto, K., Otkin. A. J., Liu, Z., Han, W., and Wang, P.: Satellite All-sky Infrared Radiance Assimilation: Recent Progress and Future Perspectives, Adv. Atmos. Sci., 39, 9-21, doi: 10.1007/s00376-021-1088-9, 2022

Lu, Q., Hu, J., Wu, C., Qi, C., Wu, S., Xu, N., Sun, L., Li, X., Liu, H., Guo, Y., An, D., and Sun, F.: Monitoring the performance of the Fengyun satellite instruments using radiative transfer models and NWP fields, J. Quant. Spectrosc. Radiat. Transf., 10.1016/j.jqsrt.2020.107239, 2020.

370   Matricardi, M.: The generation of RTTOV regression coefficients for IASI and AIRS using a new profile training set and a new line-by-line database. ECMWF, Technical Memorandum, 47 pp, doi:10.21957/59u3oc9es, 2008.

Mathiesen, P. and Jan, K.: Evaluation of numerical weather prediction for intra-day solar forecasting in the continental United States, Sol. Energy, 85(5), 967-977, doi: 10.1016/j.solener.2011.02.013, 2011.

Mayer, B., and Kylling, A.: Technical note: The libRadtran software package for radiative transfer calculations—description

375   and examples of use, Atmos. Chem. Phys., 5, 1855–1877, doi: 10.5194/acp-5-1855-2005, 2005.

Noh, Y.-C., Choi, Y., Song, H.-J., Raeder, K., Kim, J.-H., and Kwon, Y.: Assimilation of the AMSU-A radiances using the CESM (v2.1.0) and the DART (v9.11.13)–RTTOV (v12.3), Geosci. Model Dev., 16, 5365–5382, doi: 10.5194/gmd-16-5365-2023, 2023.

Omar, A. H., Winker, D. M., Vaughan, M. A, Hu, Y., Trepte, C. R., Ferrare, R. A., Lee, K.-P., Hostetler, C. A., Kittaka, C.,

380   Rogers, R. R., Kuehn, R. E., and Liu, Z.: The CALIPSO automated aerosol classification and lidar ratio selection algorithm, J. Atmos. Ocean. Technol., 26(10), 1994-2014, doi: 1994-2014.10.1175/2009JTECHA1231.1, 2009.

Ricchiazzi, P., Yang, S.R., Gautier, C., and Sowle, D.: SBDART: a research and teaching software tool for plane-parallel radiative transfer in the Earth's atmosphere, B. Am. Meteorol. Soc., 79 (10), 2101-2114, doi: 10.1175/1520-0477(1998)079<2101:SARATS>2.0.CO;2, 1998.

385 Scheck, L., Weissmann, M., and Bernhard, M.: Efficient Methods to Account for Cloud-Top Inclination and Cloud Overlap in Synthetic Visible Satellite Images, J. Atmos. Ocean. Tech., 35, 665-685, doi: 10.1175/JTECH-D-17-0057.1, 2018.

Shen, X., Wang, J., Li, Z., Chen, D., and Gong, J.: China's independent and innovative development of numerical weather prediction, Acta Meteorologica Sinica, 78(3): 451-476, doi: 10.11676/qxxb2020.030, 2020.

Tewari, M., Chen, F., Wang, W., Dudhia, J., LeMone, M.A., Mitchell, K., Ek, M., Gayno, G., Wegiel, J., and Cuenca, R:

390 Implementation and verification of the unified NOAH land surface model in the WRF model, In Proceedings of the 20th Conference on Weather Analysis and Forecasting/16th Conference on Numerical Weather Prediction. Seattle, WA, USA, pp. 11–15, 2004.

Thompson, G., Rasmussen, R. M., and Manning, K.: Explicit forecasts of winter precipitation using an improved bulk microphysics scheme. Part I: Description and sensitivity analysis, Mon. Wea. Rev., 132(2), 519–542. doi:

395 10.1175/1520-0493(2004)132%3C0519:EFOWPU%3E2.0.CO;2, 2004.

Várnai, T., and Marshak, A.: Statistical Analysis of the Uncertainties in Cloud Optical Depth Retrievals Caused by Three-Dimensional Radiative Effects, J. Atmos. Sci., 58, 1540-1548, doi: 10.1175/1520-0469(2001)058<1540:SAOTUI>2.0.CO;2, 2001.

Vidot, J., Brunel, P., Dumont, M., Carmagnola, C., and Hocking, J.: The VIS/NIR Land and Snow BRDF Atlas for RTTOV:

400 Comparison between MODIS MCD43C1 C5 and C6, Remote Sens., 10, 21, doi:10.3390/rs10010021, 2018.

Vidot, J., and Borbás, É.: Land surface VIS/NIR BRDF atlas for RTTOV-11: model and validation against SEVIRI land SAF albedo product, Q. J. R. Meteorol. Soc., 140, 2186-2196, doi: 10.1002/qj.2288, 2014.

Wang, C., Tang, G. and Gentine, P.: PrecipGAN: Merging microwave and infrared data for satellite precipitation estimation using generative adversarial network, Geophys. Res. Lett., 48, e2020GL092032, doi:10.1029/2020GL092032, 2021.

405 Xu, D., Zhang, X., Liu, Z., and Shen, F.: All-sky infrared radiance data assimilation of FY-4A AGRI with different physical parameterizations for the prediction of an extremely heavy rainfall event, Atmos. Res., 293, 106898, doi: 10.1016/j.atmosres.2023.106898, 2023.

Yang, J., Zhang, Z., Wei, C., Lu, F., and Guo, Q.: Introducing the New Generation of Chinese Geostationary Weather Satellites, Fengyun-4, B. Am. Meteorol. Soc., 98, 1737-1658, doi: 10.1175/BAMS-D-16-0065.1, 2017.

410 Yao, B., Liu, C., Yin, Y., Zhang, P., Min, M., and Han, W.: Radiance-based evaluation of WRF cloud properties over East Asia: Direct comparison with FY-2E observations, J. Geophys. Res. Atmos., 123, 4613–4629, doi: 10.1029/2017JD027600, 2018.

Zhang, J., Ma, S., Chen, D., and Huang, L.: The improvements of GRAPES_TYM and its performance in northwest Pacific ocean and South China sea in 2013, J. Trop. Meteorol., 33(1), 64-73, doi: 10.16032/j.issn.1004-4965.2017.01.007, 2017.

Zhang, X., Xu, D., Liu, R., Shen, F.: Impacts of FY-4A AGRI Radiance Data Assimilation on the Forecast of the Super

415   Typhoon "In-Fa" (2021), Remote Sens., 14(19), 4718, doi: 10.3390/rs14194718, 2022.

Zhou, Y., Liu, Y., Huo, Z., and Li, Y.: A preliminary evaluation of WRF (ARW v4.1.1)/DART (Manhattan release

v9.8.0)-RTTOV (v12.3) in assimilating satellite visible radiance data for a cyclone case, Geosci. Model Dev., 15, 7397-7420,

doi: 10.5194/gmd-15-7397-2022, 2022.

Zhou, Y., Liu, Y., and Han, W.: Demonstrating the potential impacts of assimilating FY-4A visible radiances on forecasts of

420   cloud and precipitation with a localized particle filter. Mon. Wea. Rev., 151, 1167-1188, doi: 10.1175/MWR-D-22-0133.1,

2023.

Zhou, Y., Sun, X., Mielonen, T., Li, H., Zhang, R., Li, Y., and Zhang, C.: Cirrus cloud optical thickness and effective diameter

retrieved by MODIS: Impacts of single habit assumption, 3-D radiative effects, and cloud inhomogeneity, J. Geophys. Res.

Atmos., 123(2), 1195-1210, doi:10.1002/2017JD027232, 2018.

425   Zhou, Y., Sun, X., Zhang, C., Zhang, R., Li, Y., and Li, H.: 3D aerosol climatology over East Asia derived from CALIOP

observations, Atmos. Environ., 152, 503-518, doi: 10.1016/j.atmosenv.2017.01.013, 2017.

Zinner, T., and Mayer, B.: Remote sensing of stratocumulus clouds: Uncertainties and biases due to inhomogeneity, J.

Geophys. Res., 111, D14209, doi:10.1029/2005JD006955, 2006.

Zou, X., Zhuge, X., and Weng, F.: Characterization of Bias of Advanced Himawari Imager Infrared Observations from NWP

430   Background Simulations Using CRTM and RTTOV, J. Atmos. Ocean. Technol., 33(12), 2553-2567, doi:

10.1175/JTECH-D-16-0105.1, 2016.